Nanoscale

Accepted Manuscript

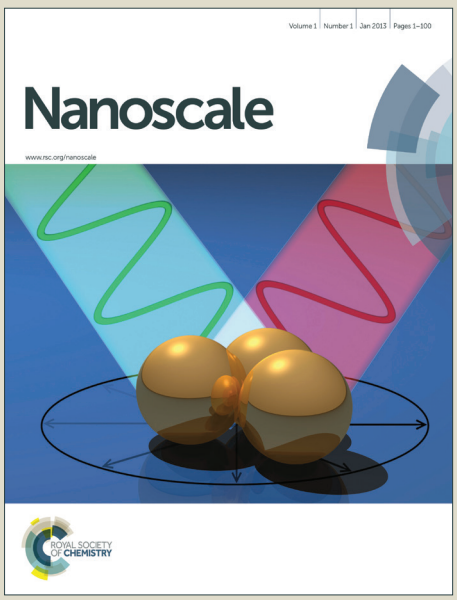

ROYAL SOCIETY OF CHEMISTRY

www.rsc.org/nanoscale

Journal Name

ARTICLE TYPE

Cite this: DOI: 10.1039/xxxxxxxxxx

Shape Effect in Cellular Uptake of PEGylated Nanoparticles: Comparison between sphere, rod, cube and disk†

Ying Li,[a] Martin Kröger,[b] and Wing Kam Liu[a*‡]

Received Date
Accepted Date

DOI: 10.1039/xxxxxxxxxx

www.rsc.org/journalname

The size, shape, surface property and material composition of polymer-coated nanoparticles (NPs) are four important parameters in designing efficient NP-based carriers for targeted drug delivery. However, due to the complex interplay between size, shape and surface property, most studies lead to ambiguous descriptions of the relevance of shape. To clarify its influence on the cellular uptake of PEGylated NPs, large scale molecular simulations have been performed to study differently shaped convex NPs, such as sphere, rod, cube and disk. Comparing systems with identical NP surface area, ligand-receptor interaction strength, and grafting density of the polyethylene glycol, we find that the spherical NPs exhibit the fastest internalization rate, followed by the cubic NPs, then rod- and disk-like NPs. The spherical NPs thus demonstrate the highest uptake among these differently shaped NPs. Based on a detailed free energy analysis, the NP shape effect is found to be mainly induced by the different membrane bending energies during endocytosis. The spherical NPs need to overcome a minimal membrane bending energy barrier, compared with the non-spherical counterparts, while the internalization of disk-like NPs involves a strong membrane deformation, responsible for a large free energy barrier. Besides, the free energy change per tethered chain is about a single k_BT regardless of NP shape, as revealed by our self-consistent field theory calculations, where k_B and T denote Boltzmann constant and temperature, respectively. Thus, the NP shape only plays the secondary role in the free energy change of grafted PEG polymers during internalization. We also find that star-shaped NPs can be quickly wrapped by the cell membrane, similar to their spherical counterparts, indicating star-shaped NPs can be used for drug delivery with high efficacy. Our findings seem to provide useful guidance in the molecular design of PEGylated NPs for controllable cellular uptake and help establish quantitatively rules in designing NP-based vectors for targeted drug delivery.

1 Introduction

Freely administrated drug molecules cannot be efficiently delivered into diseased cells to treat physiological disorders due to sequestration in the reticulo-endothelial system,[1,2] cellular uptake by immune cells,[3,4] and degradation by protein adsorption.[5] The accumulation of these freely administered drug molecules in tumors is usually at levels $\leq$ 0.1% of the injected dose per gram tissue (% ID/g).[6] However, when these molecules are encapsulated into liposomes, for example, the peak drug accumulation can be increased by one to two orders of magnitude.[7] To date, several classes of nanoparticles (NPs) have demonstrated promising properties as therapeutic carriers. By loading the drug molecules into these NPs, their pharmacokinetics, toxicity and bio-distribution can be significantly improved, compared with their freely administered counterparts.[8–11] They have been shown to efficiently deliver drug molecules into diseased cells to treat numerous physiological disorders.[8–13]

In the design of efficient therapeutic carriers for targeted drug delivery, the size and shape of NPs have been identified as two of the most important factors. Jain and co-workers found that liposomes and latex beads with diameters smaller than 300 nm could accumulate more efficiently in the tumor tissues than larger beads via the enhanced permeation and retention (EPR) effect.[14,15] Chan and co-workers studied the membrane receptor internationalization of gold (Au) and silver NPs with diameters ranging from 2 to 100 nm, and found the most efficient uptake occurring

[a] Department of Mechanical Engineering, Northwestern University, Evanston, IL 60208
[b] Department of Materials, Polymer Physics, ETH Zurich, CH-8093 Zurich, Switzerland
† Electronic Supplementary Information (ESI) available: the ESI contains additional simulation data, derivations, and relationships quoted in the main part of this work. See DOI: 10.1039/b000000x/
* Corresponding author. EMAIL: w-liu@northwestern.edu. TEL: +1-847-491-7094. FAX: +1-847-491-3915. ‡ Distinguished Scientists Program Committee, King Abdulaziz University (KAU), Jeddah, Saudi Arabia.

within 25-50 nm size range.[16] They also found that the intracellular uptake of a rod-shaped Au NP is significantly lower than that for a spherical one.[17] In short, the intracellular uptake of NPs is both size- and shape-dependent.[3,14–19] These so-called 'naked' NPs are poorly soluble in water and aggregate under physiological conditions. More importantly, *in vivo* experimental data show that these NPs are rapidly cleared after injection due to opsonization.[20]

To circumvent these issues, NP surfaces are often coated with end-grafted polymer chains, such as polyethylene glycol (PEG), which is hydrophilic and known as biocompatible, because its properties lead to protein rejection, nonimmunogenicity, and nonantigenicity. After PEGylation, the properties of NPs are dramatically changed since the surfaces of NPs are shielded by the tethered chains, allowing the NPs to be well dispersed in solution. The PEG outer shell of these NPs can dramatically reduce the protein opsonization on their surface and the subsequent phagocytosis by the immune system, eventually elongating their circulation time.[4,21,22] To enhance cellular uptake of PEGylated NPs, the targeting moieties (ligands) are usually covalently bound to the free ends of tethered chains, and can specifically and firmly bind to receptors over the surface of the diseased cell.[23–26] Interestingly, the pharmacokinetic behavior, bio-distribution and cellular uptake of these PEGylated NPs are also found to be dependent on the size and shape of NPs, revealed by experimental studies.[22–27] The smaller sized PEGylated NPs are found to be more easily accepted by the diseased cells through *in vitro* experiments, compared with their larger counterparts,[26] which has been further confirmed by our large scale molecular simulations.[28] The shape and surface functional group of PEGylated NPs are also identified to affect their adsorption and internalization behaviors.[26] Nevertheless, due to the interplay between size, shape and surface properties of NPs, especially for PEGylated NPs, most experimental studies lead to ambiguous descriptions of NP shape effect. There are two reasons for this problem: (i) differently shaped NPs have different surface area-to-volume ratios, which makes discerning size effect from surface effect difficult, especially when only a few different shapes are considered; and (ii) differently shaped NPs usually have different grafting densities of PEG polymers due to their different surface curvatures.[29] For instance, the coverage density of PEG polymers is only about 0.052 chains/nm^2 for rod-shaped Au NPs, while it has been dramatically increased to 1.63 chains/nm^2 for spherical Au NPs, under the same experimental condition.[29] Therefore, the difference of tethered PEG densities leads to the different intracellular behaviors of these NPs, preventing the accurate understanding of the relevance of shape.

To clarify the role of NP shape during the cellular uptake of PEGylated NPs, we performed large scale dissipative particle dynamics (DPD) simulations, which has been proven to serve as an efficient and accurate method to study the internalization of PEGylated spherical NPs.[28] We start with spherical NPs, then study the rod and other shaped convex NPs that have in common an identical surface area and grafting density. Such precisely defined conditions will allow us to unambiguously explore the shape effect of NPs during internalization. Note that such a controlled state with known size, shape and surface property of

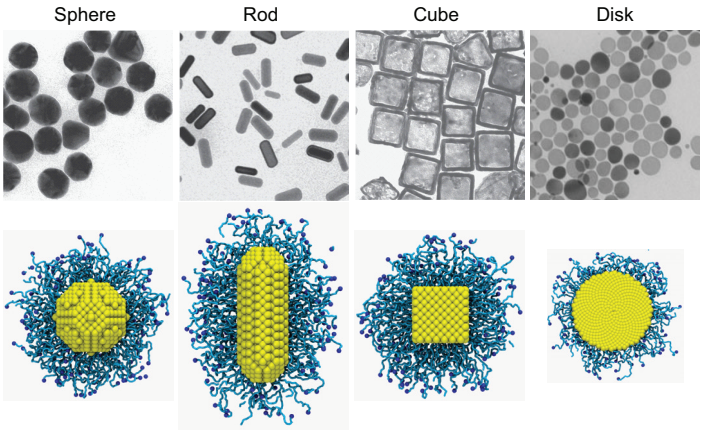

Fig. 1 Differently shaped NPs: sphere, rod, cube and disk. The top shows the transmission electron microscopy images of these NPs, reproduced with permission from Refs.[29,30] The bottom shows the PEGylated NPs with grafting density 1.6 chains/nm^2 in our molecular simulations. The cores of PEGylated NPs are colored yellow. The tethered PEG polymers and targeting moieties are represented by cyan lines and blue beads, respectively. To clearly reveal the shape of different cores, only half of tethered chains (partially hidden by the core) are shown.

NPs can only be explored through computational studies, in an attempt to provide guidance on the design and fabrication of NPs to achieve better efficacy in targeted drug delivery. In studying the shape effect of PEGylated NPs, we consider four NPs geometries: spheres, which account for the majority of documented NP systems, rods, cubes and disks, as depicted in Fig. 1. Both sphere and cube have all their three dimensions of comparable length, while they differ in their number of edges and corners. The (prolate) cylindrical rod has one long axis of symmetry and two short half axes. The (oblate) circular disk has one dimension shorter than the other two. In this way, these differently shaped NPs have very different aspect ratios. The cubic NP is chosen since the Au nanocages have many unique features made them attractive in nanomedicine.[31] Our molecular simulation results reveal that spherical NPs demonstrate the highest endocytosis rate, followed by cubic NPs, rod- and disk-like NPs. Thus, the spherical NPs are the most efficient therapeutic carriers among these differently shaped NPs, since they encounter minimal membrane bending energy during endocytosis, comparing with other differently shaped counterparts. For NPs with high aspect ratios, such as rod and disk, their internalization rates are found to be highly dependent on the entry angle, and delayed by the large deformation of membrane and complicated rotation of these NPs. We also find that star-shaped NPs can be quickly wrapped by the cell membrane, similar to their spherical counterparts, indicating star-shaped NPs can be used for drug delivery with high efficacy.

Note that endocytosis is a process during which the cell internalizes molecules, such as proteins and other macromolecules, via a deformation of its cell membrane and an accompanying generation of membrane-bound carriers.[32,33] The typical endocytotic pathway of a NP consists of four fundamental steps:[32] (1) specific binding of the NP to the cell surface; (2) membrane wrapping

around the NP and formation of a membrane-bound NP carrier; (3) pinching-off of the membrane budding to form an early stage endosome; (4) endosomal release of the NP during the late state of the endosome. The present study focuses on the critical and necessary conditions for the NPs to be delivered into the interior of the cell, characterized by steps (1) and (2). Steps (3) and (4) concerning the endosomal release of NPs therefore remain beyond the scope of the present study.

This paper is organized as follows. Section 2 describes the DPD simulation models for PEGylated NPs and cell membrane, and corresponding technique for studying internalization of PEGylated NPs. The self-consistent field theory is also introduced to study the free energy of tethered PEG polymers. Section 3 contains the internalization pathway of different PEGylated NPs and compares the different internalization rates induced by the shape effect. The free energy change of grafted PEG chains during endocytosis is quantified through self-consistent field theory. Section 4 discusses the NP shape effect during endocytosis and compares the simulations results with existing experimental and computational observations. Finally, section 5 concludes the present study.

2 Model and methodology

2.1 DPD simulation technique

The DPD simulation is a coarse-grained method for stochastic simulating the dynamics and rheological properties of soft materials with correct hydrodynamic interactions.[34,35] In the DPD model, each bead represents several atoms, whole molecules or fluid regions, rather than single atoms, thus, atomistic details are considered to be irrelevant to the process addressed. The degree of freedom for the beads in the system are integrated according to Newton's equations of motion, supplemented by simplified pairwise dissipative and random forces. The momentum is locally conserved to ensure correct hydrodynamic behavior. The DPD method allows us to access longer time and length scales compared with those that cannot be approached by conventional molecular dynamics simulations. A detailed description of the DPD method and parameterization can be found in our previous study for PEGylated spherical NPs[28] and Electronic Supplementary Information (ESI) section 1. Here we just briefly describe the model and methodology for completeness.

The DPD simulation technique has been successfully applied to study the behaviors of cell membranes.[36–40] Here we adopt the lipid model developed by Groot and Rabone.[36] The lipid molecule is simplified as $H_3(T_5)_2$ amphiphile, where H and T representing the hydrophilic lipid heads and hydrophobic lipid tails, respectively. The lipid head and tail are denoted by ice-blue beads and silver lines (cf. simulation snapshots given in Figs. 3-4), respectively. Adjacent beads are connected via a harmonic spring. To maintain the chain rigidities of the lipid head and tail, a harmonic potential is applied for all bond angles in the lipid molecule. In this way, the dynamics, bending modules and viscosity of the self-assembled lipid bilayer are found to be in good agreement with experimental measurements.[36,39] Such a model has been widely used to study the translocation and internalization of different NPs.[28,37,38,40–43] According to previous studies,[44–46] we assume that 50% of lipids randomly distributed within the bilayer are coated with receptors to accelerate the simulations, which has been found to be a useful estimate. Especially, the endocytic kinetics can be quantitatively captured by these accelerated simulations.[37,44–46] The heads of these lipids have attractive interactions with targeting moieties covalently conjugated to the free ends of tethered PEG chains on NP surfaces, providing the specific ligand-receptor interactions.[28]

During the DPD simulation for cellular uptake of PEGylated NPs, the lateral tension of the lipid bilayer is maintained to be zero, for mimicking a real cell membrane with large surface area-to-volume ratio. The N-varied DPD method[47] is adopted to maintain the lateral tension, by monitoring the lipid number per area (LNPA), rather than the lateral force/pressure. The LNPA of the boundary region is kept constant at a value denoted as ρ_c, thus, the boundary region behaves like a reservoir. When the LNPA of the boundary is larger than ρ_c, the additional lipid molecules in this region are deleted and a corresponding number of solvent beads is simultaneously added. When the LNPA is smaller than ρ_c, extra lipid molecules are added and the same amount of solvent beads is deleted instantaneously. The LNPA of the boundary region is checked every 1000 time steps to ensure the zero lateral tension of the lipid bilayer and allow it to be relaxed. In this way, the N-varied DPD method enables us to control the lateral tension of the membrane and provides extra membrane area to release the tension during the endocytosis of PEGylated NPs. Such a method has been successfully utilized to understand the budding behavior of a multicomponent membrane,[47] the cellular uptake of ligand-decorated rigid NPs,[48] dendrimer-like soft NPs,[38] and PEGylated spherical NPs.[28] In accord with previous studies on the relationship between LNPA and lateral tension of the membrane,[36,38,41] $\rho_c = 1.1022$ is chosen to ensure that the lateral tension vanishes permanently during the coarse of our dynamic simulations.

The cores of differently shaped convex NPs, except for disk, are cut from a bulk of beads arranged on a FCC lattice (Fig. 1) with lattice constant 0.90 nm. The disk is formed by beads uniformly distributed in a circle with one bead thickness, since the cut from the FCC lattice cannot accurately maintain the circular shape. The close packing of these beads prevents the water and other molecules to enter the interior of core during the DPD simulation. We first fix the radius $\mathscr{R}_{\text{sphere}}$ of sphere to be 4 nm, then construct other shaped NP with equal surface area. The aspect ratio of the cylindrical rod is defined as $\rho = (\mathscr{R}_{\text{rod}} + 0.5\mathscr{L}_{\text{rod}})/\mathscr{R}_{\text{rod}}$, where $\mathscr{R}_{\text{rod}}$ and $\mathscr{L}_{\text{rod}}$ are the radius of the hemispherical caps at two ends and length of cylindrical part, respectively. Here we fix the aspect ratio ρ to be 3, which has been widely used in both experiments[17] and simulations.[44,49] Thus, the radius $\mathscr{R}_{\text{rod}}$ and length $\mathscr{L}_{\text{rod}}$ of the rod are 2.31 and 9.23 nm, respectively. The side length $\mathscr{L}_{\text{cube}}$ of the cube and radius $\mathscr{R}_{\text{disk}}$ of the disk are 5.79 and 5.66 nm, respectively. In this way, the surface area of the core (the tethering surface) for differently shaped NPs is kept constant at $A_{\text{surf}} = 201$ nm^2. The cores of spherical, rod-like, cubic and disk-like NPs are formed by 1566, 1272, 1098 and 522 beads, respectively. Note that we choose to maintain the equal surface area for differently shaped NPs, instead of the surface area-to-volume

ratio. There are two reasons for this choice: 1) the drug molecule loading capacity of NPs often relies on their surface areas, and 2) the NPs are coated with the same amount of PEG monomers under the same grafting density. More importantly, all the free ends of tethered chains are conjugated with ligands, by mimicking the experimental conditions.[25,26] Under the constraints of equal surface area and grafting density, all these NPs will have the same ligand-receptor binding strength, allowing us to unambiguously explore the shape effect during endocytosis. The beads forming the NP core move as a rigid body during the DPD simulations.

A coarse-grained model has been adopted to model the PEG polymers in our DPD simulations.[50] Each monomer of PEG has been simplified as a single bead. All the beads on the PEG chain are consecutively connected by harmonic springs and the chain stiffness is maintained by using the proper bond angle interaction, also given by a harmonic potential. Such a polymer model accurately captures the conformation (such as end-to-end distance and radius of gyration) of PEG polymers in water environment with different molecular weights, as demonstrated previously.[28] The interaction parameters between PEG and lipid molecules have been calibrated through experimental results by Groot and Rabone.[36] During the DPD simulations, the PEG chains are tethered on randomly selected, but distinct surface beads of the core at the given grafting density σ_p. According to existing experimental studies,[24,51,52] the typical grafting density of PEG ranges from 0 (ungrafted) to 2.0 chains/nm^2. Thus, we choose a homologous series of grafting densities $\sigma_p = 0.2$, 0.4, 0.6, 0.8, 1.0, 1.2, 1.4 and 1.6 chains/nm^2 to explore the grafting density effect. The corresponding integer-valued numbers of grafted PEG chains are $M = \sigma_p A_{\text{surf}} = 40$, 80, 121, 161, 201, 241, 281 and 322 for all shapes. The typical molecular weight of a grafted PEG polymer is about 550–5000 Da, corresponding to polymerization degree $N_p = 12$–112.[24–26,52] Taking into account the computational cost, we choose N_p to be 30 in our simulation, representing the molecular weight of PEG as 1358 Da. The possible effect of N_p has been explored in our previous study on PEGylated spherical NPs with $N_p = 18$ and 36.[28] The wrapping time during endocytosis will be enlarged (reduced) with longer (shorter) grafted PEG polymers.[28] All the PEG chains are randomly and covalently tethered to the surfaces of the NPs. To ensure that tethered chains do not detach from the NP surface during endocytosis, each tethered PEG monomer is covalently bound to a surface bead of the NP via the same harmonic bond potential used to covalently bind PEG monomers (ESI section 1).

According to the experimental study by Xia and co-workers,[26] the measured Zeta-potential of PEGylated NP is fairly small (between -2 and 0 mV), indicating a very weak electrostatic interaction. Thus, we do not consider electrostatic interactions in the present study. They have been ignored in previous related studies as well.[37,44–46]

After PEGylation, the interaction strength between NP and cell surface has been dramatically reduced due to the non-specific steric interaction induced by the tethered chains. Therefore, the cellular uptake of PEGylated NPs is prohibited because the NP-membrance interaction cannot overcome the steric hindrance of tethered PEG.[26] To enhance the specific cellular uptake of PEGylated NPs, the free ends of grafted PEG are typically conjugated with targeting moieties, such as anti-HER2 antibodies[26] or arginylglycylaspartic acid (RGD) peptides[25,53] These conjugated targeting moieties can specifically recognize and bind with receptors expressed over the surface of a diseased cell. To mimic this effect of enhanced internalization via specific ligand-receptor interactions in DPD simulations, we assume all the free ends of tethered chains to be bound with targeting moieties, which have attractive interactions with receptors coated on the heads of lipids.[28] Such an attractive interaction is implement through a modified Lennard-Jones potential with cutoff radius r_c, which has been widely used in the computational works to mimic the specific ligand-receptor interactions.[28,44,45,54] In this work, the ligand-receptor interaction strength F_{LR} has been fixed to be 7.65 $k_{\text{B}}T$, where k_{B} is the Boltzmann constant and T is the temperature, which is within the typical range of ligand-receptor interaction strength measured from experiments and detailed all-atomistic simulations (6.5 to 20 $k_{\text{B}}T$).[55]

In our DPD simulation, the mass, length, and time scale are all normalized. The unit of length is taken to be the cutoff radius r_c. The unit of mass m is that of the solvent beads. The unit of energy is taken to be $k_{\text{B}}T$. Then, all other quantities are given in terms of these basic units. The velocity-Verlet integration algorithm is adopted and the simulation time step is $\delta t = 0.01\tau$ with $\tau = (mr_c^2/k_{\text{B}}T)^{1/2}$. The reduced DPD units can be readily converted into SI units by mapping the membrane thickness and lipid diffusion coefficient from DPD simulation results to experimental measured values. The simulated lipid bilayer thickness is about $5r_c$. By comparing with the experimentally measured thickness for 1-palmitoyl-2-oleoyl-sn-glycero-3-phosphocholine (POPC) bilayer, which is about 4 nm,[56] the basic length unit in the DPD simulation is about $r_c \simeq 0.8$ nm. By mapping the diffusion coefficient around 5 μm^2/s for POPC bilayer,[56] the time unit in the DPD simulation is about $\tau = 24.32$ ps. The lateral dimension of the lipid bilayer is about 41×41 nm, which has been proven large enough to avoid finite system size effect.[28]

2.2 Self-consistent field theory

To interpret and make use of the DPD simulation results, we employ an independent self-consistent field (SCF) theoretical approach to estimate the volume fraction profiles for each of the N_p monomers separately along a representative tethered chain, i.e. along the surface normals. The SCF result allows us to calculate the radial volume fraction profile $\phi(r)$ of the spherical, polymeric brush, the volume fraction profile of the terminal monomers, $\phi_{N_p}(r)$, and the corresponding free energy, F_{poly}. We find that the measured PEG profiles of the unwrapped NPs are recovered using a simplest classical, parameter-free model of a polymer under good solvent conditions, that is characterized by a dimensionless mixing free energy density $vf_m(\phi) = \tau\phi^2 + w\phi^3$ with $\tau = w = 1$, where $v = 0.0633$ nm^3 denotes the excluded volume of a PEG monomer.[57] Within the SCF we basically aim at minimizing a single chain *free energy functional* $F_{\text{poly}}[\phi(\mathbf{r})] = F_{\text{el}} + F_{\text{int}}$ that is

composed of an elastic and interaction part,[28]

$$\frac{F_{\rm poly}[\phi(\mathbf{r})]}{k_{\rm B}T} = \frac{3}{2}\frac{\langle r^2\rangle}{R_0^2} + \int_V f_m(\phi)\, d^3r, \qquad (1)$$

where $\langle r^2\rangle \equiv V^{-1}\int (r-\mathscr{R}_{\rm sphere})^2\phi\, d^3r$ is the mean squared extension of a polymer normal to the tethering surface, that is tethered on a sphere of radius $\mathscr{R}_{\rm sphere}$, properly normalized by the occupied chain volume $V = \int \phi d^3r = N_p v$. The quantity $R_0 = R_0(N_p)$ stands for the equilibrium size of a PEG polymer, that is intermediate between its gyration radius and mean squared end-to-end distance. We employ $R_0^2 = \langle R_{\rm ee}^2\rangle/e$ using the available $\langle R_{\rm ee}^2\rangle(N_p)$ values for a single PEG chain in water.[28] In the above equation, the first term $F_{\rm el} = 3\langle r^2\rangle/2R_0^2$ characterizes the entropy-dominated elastic free energy of tethered chains, representing compression/stretching of these chains relative to their equilibrium size R_0. The interaction energy between different chains is given by the integrated mixing free energy density $F_{\rm int} = \int_V f_m(\phi)\, d^3r$. It is worthwhile mentioning that there are additional contributions to the free energy of the NP-membrane complex, such as rigid-body translational and rotational entropy retained by the NP, when internalized by a membrane,[58] or the bending energy cost of the membrane (to be discussed below). Additional contributions to the free energy of the complex may also originate from the introduction of new vibrational modes in the wrapped state. In an attempt to interpret the DPD simulation results we have chosen to monitor the variation of the above free energy contributions that suffice to determine the polymer (and monomer) density profile of the coated NPs in their unwrapped state.

The above free energy (eq 1) has to be minimized with respect to the volume fraction profile, subject to the constraints of conserved V and the tethering condition, $\phi(r<\mathscr{R}_{\rm sphere}) = 0$. A more detailed introduction to the SCF can be found in Refs.[59–62] A most common numerical implementation of the related optimization problem on a geometry-adapted grid had been introduced by Scheutjens and Fleer.[59] We follow the implementation described for the case of a sphere in detail by Wijmans and Zhulina.[63] To this end, a single flexible polymer is grown sequentially, using a constant bond length $a = 0.33$ nm (for PEG), starting from a spherical surface of radius $\mathscr{R}_{\rm sphere}$. During (a priori) random growth within the space surrounding the NP, the representative chain creates its own radial volume fraction profile (with multiplicity of the number of tethered chains, recorded within spherical shells of thickness a) to which it reacts, as the volume fraction enters the probability to choose from all possible directions, at each step of the growth procedure. To be precise, it reacts by its current radial coordinate r to the dimensionless chemical potential $U(\phi)/k_{\rm B}T = v f_m'(\phi) = 2\phi + 3\phi^2$ contained in a segment weighting factor $G_1(r) = \exp(-U(r)/k_{\rm B}T)$, where we recall that $\phi = \phi(r)$. The problem is thus closely related to a diffusion process in the presence of a potential and boundary, and can in principle also be formally treated using Green's functions.[64] Accordingly, one introduces $G_n(r)$, the average statistical weight of an n-mer of which the last segment is located in layer r: $G_n(r) = \langle G_{n-1}(r)\rangle\, G_1(r)$ for $n = 2,\ldots,N_p$, where the spatial average is taken over a sphere of radius a, centered at r. We are left with a closed set of coupled equations, where the averages play the role of the coefficients of a linear system of equations that can be solved in an iterative fashion using simple matrix inversions. Due to head-tail symmetry of the polymer chains, the volume fraction profile of an n-mer is subsequently obtained from the solution $G_n(r)$ via $\phi_n(r) = C_n G_n(r) G_{N-n+1}(r)/G_1(r)$, where the C_n's are normalization factors that follow from $v = \int \phi_n(r) d^3r$ and finally $\phi(r) = \sum_{n=1}^{N}\phi_n(r)$ as well as $\phi_{N_p}(r)$ are obtained. The method is readily adapted to handle arbitrary geometries. Because the volume fraction profiles $\phi_n(r)$ of the unwrapped PEGylated NPs are all well recovered, we can estimate the free energy difference $F_{\rm poly}$ between wrapped and unwrapped PEGylated NP upon inserting the two measured $\phi(\mathbf{r})$'s fields separately into Eq. 1.

2.3 Flory theory for tethered chains

Upon assuming a flat volume fraction profile, $\phi_0 = N_p v/V_0$, the above SCF reduces to Flory theory[65,66] that aims at minimizing a simplified *free energy function* of the form $F_{\rm poly}(R)/k_{\rm B}T = 3[R^2/R_0^2 + R_0^2/R^2] + (N_p v/\phi_0) f_m(\phi_0)$ with respect to end-to-end distance R to calculate the equilibrium brush height $R_{\rm eq}$ and corresponding equilibrium free energy $F_{\rm poly}(R_{\rm eq})$ of the PEGylated NP, and $R_{\rm eq}$ can be identified with $\langle r^2\rangle^{1/2}$. The additional term $(R_0/R)^2$ is often skipped when one is interested in scaling laws, but required to ensure $R_{\rm eq} = R_0$ in the absence of interactions (and in agreement with SCF); a better motivation is given elsewhere.[66] The additional term is only irrelevant in the strong stretching regime, characterized by $R_{\rm eq} \gg R_0$. Within the Flory approach V_0 is the mean volume accessible for a single chain. It depends on R and the NP geometry. For the spherical NP, $V_0 = (4\pi/3)[(R+\mathscr{R}_{\rm sphere})^3 - \mathscr{R}_{\rm sphere}^3]$ divided by the number of tethered chains, $M = 4\pi\mathscr{R}_{\rm sphere}^2\sigma_p$. For the other shapes see ESI section 3. As we will see below, both Flory theory and SCF are able to rationalize the brush heights and free energy contributions of the unwrapped configurations (cf. Fig. 2), but the SCF expression Eq. 1 for the energy functional is employed to calculate the free energy of the wrapped configurations from the measured spatial density profile $\phi(\mathbf{r})$, i.e. when the assumptions underlying Flory theory are certainly inappropriate.

3 Results

3.1 Conformation of PEGylated NPs

The equilibrated conformations of the PEGylated NPs are given in Fig. 1 (bottom) and ESI Figs. S1-S4. When the grafting density is low (such as 0.2 chains/nm^2), the tethered PEG chains are isolated and collapsed on the surface of the core, forming the 'mushroom' conformation to minimize the conformational entropy loss.[28] However, when the grafting density is high (such as 1.6 chains/nm^2), the tethered chains are very close to each other. To reduce their steric interactions, the grafted PEG polymers are stretched out from the NP surface, forming a 'brush' conformation. The similar mushroom-to-brush transition has also been observed for planar tethered PEG polymers with grafting density increasing from 0.015 to 1.25 chains/nm^2.[50] Interestingly, in the brush regime, especially for high grafting density, the cores of PEGylated NPs are fully shielded by tethered chains. Thus, the shape

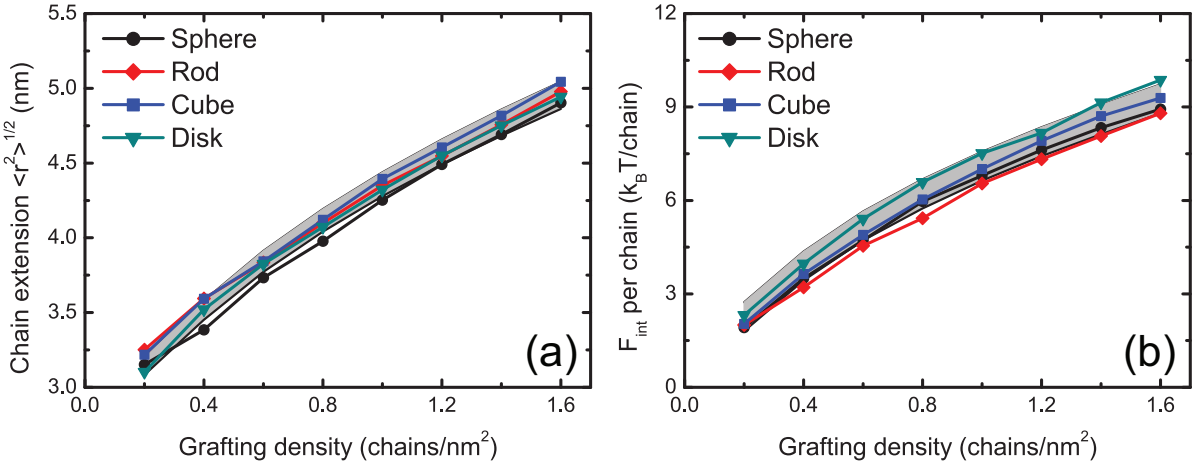

Fig. 2 Grafting density effect on (a) extension of tethered PEG chains $\langle r^2\rangle^{1/2}$ and (b) interaction free energy between tethered chains of the unwrapped NPs. See the main text for the definition of $\langle r^2\rangle^{1/2}$. The results for the four shapes obtained using SCF and Flory theory (sections 2.2 and 2.3) are fully compatible with simulation results for the elastic (a) and interaction (b) contributions to the mixing free energy, and located within a single gray stripe for better visibility of the simulation results. While the sum of elastic and interaction contributions to the free energy is located in a minimum in the unwrapped state for each value of the grafting density, the change of the SCF free energy during internalization will be monitored by analyzing the two contributions separately. The relative errors are below 5% for all data points based on 5 independent runs, which are smaller than the symbols in the figure.

of different NPs is not fully visible to the cell, which will play an important role during the internalization process (to be discussed in detail in Section 4).

To quantify the extension of the tethered chains, we use again the mean squared 'normal' distance $\langle r^2\rangle = \int r_\perp^2\,\phi(\mathbf{r})dr^3 / \int \phi(\mathbf{r})dr^3$, where $r_\perp$ is the shortest distance between a position in space and the PEGylated NP surface and $\phi(\mathbf{r})$ is the volume fraction distribution of PEG monomers at position $\mathbf{r}$. The obtained extension $\langle r^2\rangle^{1/2}$ of PEG polymers from the NP surface are shown in Fig. 2(a) for differently shaped NPs and grafting densities. With grafting density increasing from 0.2 to 1.6 chains/nm^2, the extensions of tethered chains are monotonically increasing from 3.25 to 5 nm, corresponding to the previously observed mushroom-to-brush transition. For $N_p = 30$, the end-to-end distance R_{ee} is about 3 nm for a single PEG chain in water,[28] which is close to the extension of tethered chains at grafting density 0.2 chains/nm^2. However, at high grafting density 1.6 chains/nm^2, the tethered chains are significantly stretched as their extension $\langle r^2\rangle^{1/2}$ has been increased by 54%. Interestingly, all the measured curves are compatible with the simple Flory theory of section 2.3 with our $vf_m(\phi) = (1+\phi)\phi^2$ for PEG. Since the elastic energy F_{el} of tethered chains is proportional to the extension $\langle r^2\rangle$ (the first term on the right hand side of Eq. 1), F_{el} predicted by the SCF theory is also in good agreement with the simplified Flory theory (results not shown here). The interaction energy between tethered chains F_{int}, given as the second term on the right hand side of Eq. 1, is presented in Fig. 2(b). Similar to $\langle r^2\rangle^{1/2}$, F_{int} is monotonically increasing with the increment of grafting density for differently shaped NPs, signaling the strong interaction strength between neighboring chains at high grafting density. Again, the F_{int} given by SCF theory lies in the range predicted by the Flory theory. The agreement between SCF and Flory theories on brush heights and free energy contributions of grafted PEG polymers indicates that the simple Flory theory could be used for rational design of PEGylated NPs, before they encounter the diseased cells.

3.2 Endocytic kinetics of PEGylated NPs

The receptor-mediated endocytic kinetics of PEGylated NPs are given in Figs. 3–4 and ESI Figs. S5-S8. At high grafting density 1.6 chains/nm^2 (cf. Fig. 3), all the PEGylated NPs can be rapidly accepted by the cell within 2.24–2.77 μs due to the strong ligand-receptor interactions. Initially, at $t = 0$, the PEGylated NPs are far away from the cell surface. Thus, the targeting moieties conjugated on the free ends of tethered PEG polymers are not visible to the receptors expressed over the lipid bilayer. When the PEGylated NPs approach the cell surface, the targeting moieties recognize the receptors (lipid heads) and bind with them, due to the specific ligand-receptor interactions. Simultaneously, the lipid bilayer starts to bend and wrap around the PEGylated NPs ($t \approx 0.24\ \mu s$). In the course of time, more and more receptors diffuse into the membrane bending region and bind with the targeting moieties. This stage ($0 < t < 1.70\ \mu s$) is mainly driven by the free energy release from the specific ligand-receptor binding, accompanied by the large bending of the lipid bilayer; defining the so-called 'membrane bending stage'. Afterwards, the majority of PEGylated NP is wrapped by the membrane, and the upper leaflet of the lipid bilayer starts to protrude and warp around the PEGylated NP from the top. However, the lower leaflet only bends slowly, compared with its large bending behavior during the membrane bending stage. This process dominates the 'membrane monolayer protruding stage' ($1.70\ \mu s < t < 2.50\ \mu s$). Finally, all the PEGylated NPs are fully wrapped by the lipid bilayer (at $t \approx 2.24$–$2.77\ \mu s$), and located around the center of the membrane to reduce its bending energy, reaching the 'equilibrium stage'. Such a wrapping pathway has been identified in

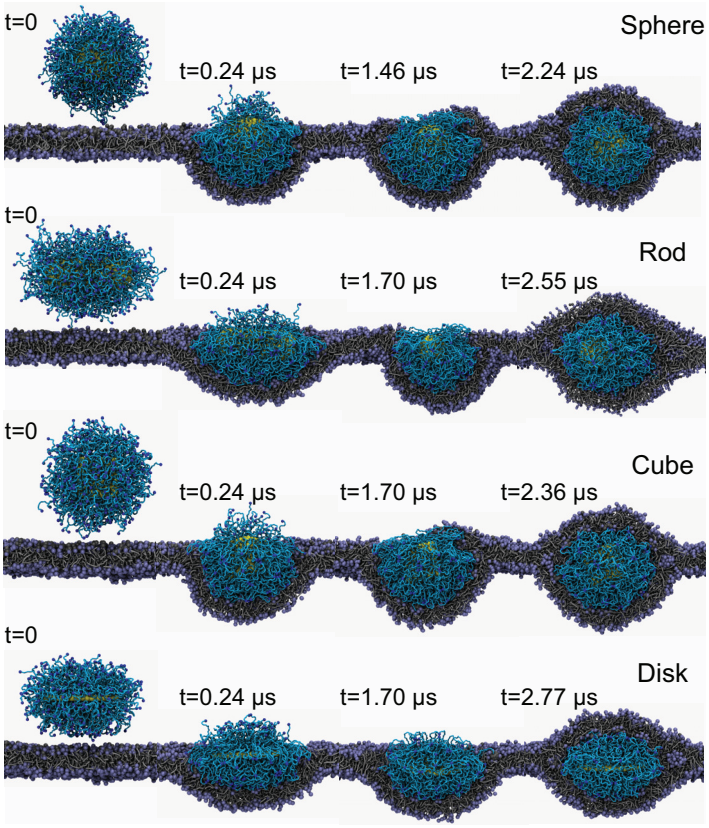

Fig. 3 Side view of the internalization pathway for PEGylated NPs with grafting density 1.6 chains/nm^2. The whole process can be classified into three stages: membrane bending stage ($0 < t < 0.24$ μs), membrane monolayer protruding stage ($0.24 < t <$ 2.24–2.77 μs) and equilibrium stage ($t >$ 2.24–2.77 μs). The lipid head and tail are denoted by the ice-blue beads and silver lines, respectively. The color scheme for PEGylated NPs is the same as Fig. 1. The water molecules are made inviable for clarity.

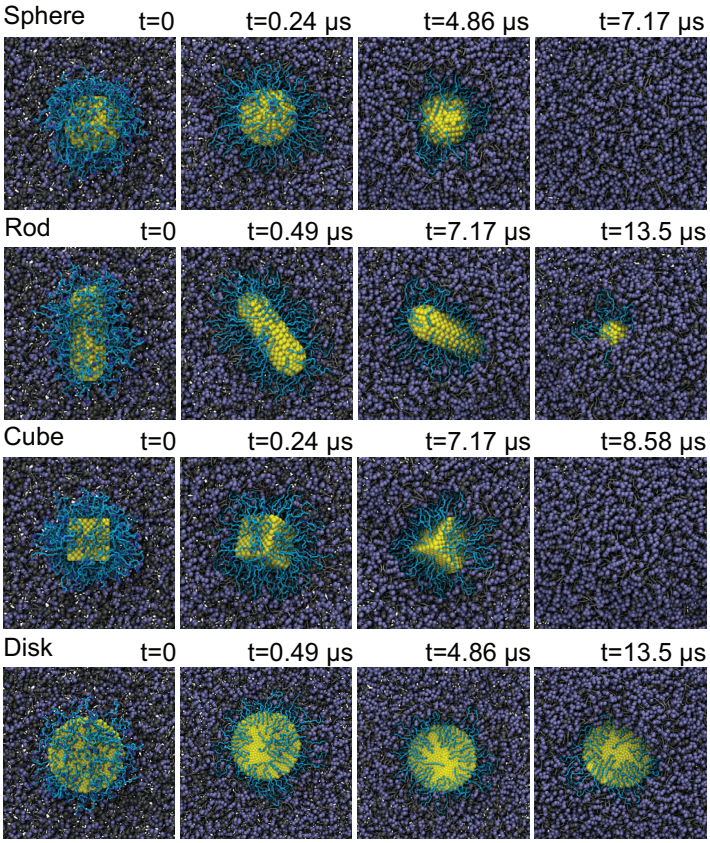

Fig. 4 Top view of the internalization pathway for PEGylated NPs with grafting density 0.6 chains/nm^2. The color scheme is the same as Fig. 3. The spherical and cubic NPs can be fully wrapped by the membrane within $t =$ 7.17–8.58 μs, while rod- and disk-like NPs cannot be fully wrapped after $t =$ 13.5 μs.

our previous studies for PEGylated spherical NPs.[28] Interestingly, the wrapping times τ_w for PEGylated NPs with different shapes to be fully internalized are very close to each other, e.g. τ_w =2.24–2.77 μs, indicating that the shape of NPs does not play an important role in this process. At this large grafting density of 1.6 chains/nm^2, the shape anisotropy of these NPs is basically hidden by tethered chains. As we'll discuss below, and further evidenced by results collected in ESI Figs. S5-S8, the densely covered NPs can effectively be replaced by a spherical brush.

At the intermediate grafting density 0.6 chains/nm^2 (cf. Fig. 4), the internalization of PEGylated NPs still follows the 'membrane bending stage', then 'membrane monolayer protruding stage' and finally 'equilibrium stage', as shown for PEGylated NPs with high grafting density 1.6 chains/nm^2. Nevertheless, the endocytic kinetics is much slower, compared with the scenario at grafting density 1.6 chains/nm^2. The wrapping time τ_w for PEGylated spherical NPs has been enlarged from 2.24 to 7.17 μs with grafting density decreasing from 1.6 to 0.6 chains/nm^2. More importantly, until 13.5 μs, rod- and disk-like NPs still cannot be fully internalized, leading to the frustrated endocytosis.[67] Although most parts of the rod-like NP have been covered by the lipids, only about 60% of disk-like NP surface has been wrapped by the membrane. Therefore, we have an indication that the shape of NP can play a very important role at this intermediate grafting density. At the very low grafting density 0.2 chains/nm^2, the overall ligand-receptor interaction strength is very weak. It cannot overcome the energy barrier created by the bending energy of the membrane and the conformational free energy loss of tethered PEG polymers. Thus, the PEGylated NPs can only adhere on the surface of the membrane, or slightly be wrapped by the membrane (cf. ESI Figs. S5-S8).

To quantify the effects of grafting density (also the density of targeting moiety) and shape on endocytic kinetics of PEGylated NPs, wrapping times τ_w required for PEGylated NPs to be fully enveloped by the membrane are given in Fig. 5(a). For differently shaped NPs, τ_w is monotonically increasing with decreasing grafting density (targeting moiety density), demonstrating the important role played by the ligand-receptor interactions.[28] The NP shape does not significantly affect the wrapping time τ_w at high grafting densities (1.4-1.6 chains/nm^2), as aforementioned, while it does play a very important role when the grafting density is smaller than 1.2 chains/nm^2. At a given grafting density, the spherical NP is quickly accepted by the cell, followed by the cubic and rod-like NPs and lastly, the disk-like NP. To further under-

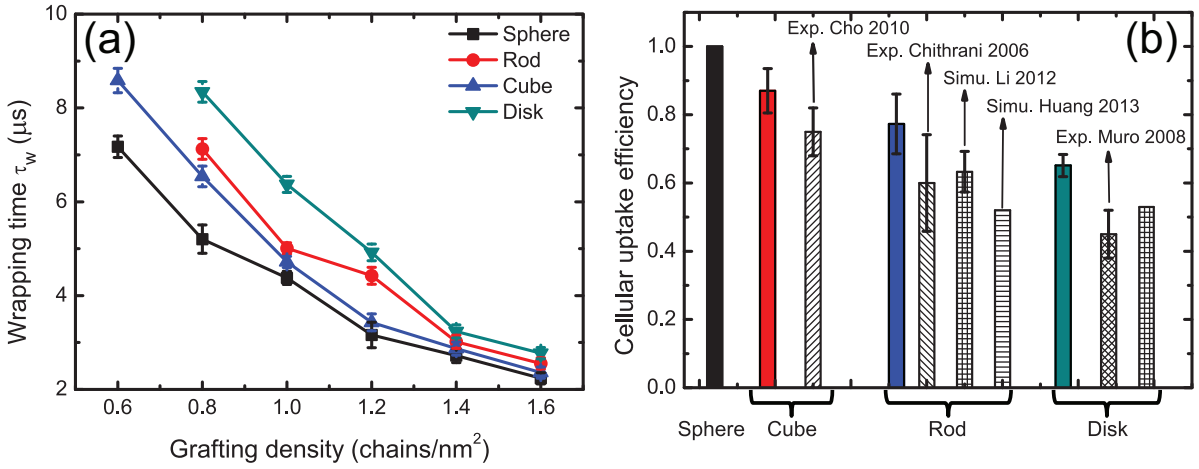

Fig. 5 NP shape effect on (a) the wrapping time τ_w required for PEGylated NPs to be fully wrapped by the membrane and (b) the cellular uptake efficiency, defined in the text part. In (a), the wrapping processes for rod- and disk-like NPs at 0.6 chains/nm^2 are very slow compared with those for the sphere and cube, and beyond our computational limit. Thus, the corresponding wrapping times are not provided. In (b), the experimental results are taken from Cho 2010,[26] Chithrani 2006,[17] and Muro 2008.[68] Previous simulation results are collected from Li 2012,[54] and Huang 2013.[49] The solid columns represent the results obtained from the present DPD simulations.

stand the NP shape effect, we choose the wrapping time τ_w^{sphere} for spherical NPs with grafting densities 0.6–1.2 chains/nm^2 as baselines. The relative cellular uptake efficiency of other shaped NPs is then defined as $\tau_w(\sigma_p)/\tau_w^{\text{sphere}}(\sigma_p)$, where $\tau_w(\sigma_p)$ is the time for the PEGylated NP with grafting density σ_p to be fully internalized. The superscript 'sphere' denotes the spherical NP. To demonstrate the NP shape effect, we only consider the grafting density $\sigma_p =$ 0.6–1.2 chains/nm^2. The cellular uptake efficiency for differently shaped NPs is given in Fig. 5(b). Along with observations already described, if the spherical NPs are considered to be 100% taken up, only 87% cubic NPs, 77% rod-like NPs, or 65% disk-like NPs can be internalized during the same amount of time. Thus, the spherical NPs have the highest cellular uptake efficiency, followed by the cubic NPs, then rod-like NPs and finally, disk-like NPs, under the same amount of ligand-receptor interaction strength and tethered PEG monomers.

3.3 Free energy change of grafted PEG polymers

During the receptor-mediated endocytosis of PEGylated NPs, there are three major free energy changes involved:[28,69] (i) the specific ligand-receptor interaction, provided by the binding between the targeting moieties conjugated on the free ends of tethered chains and receptors expressed over the membrane; (ii) the membrane bending energy, due to the lipid bilayer deformation; (iii) the non-specific steric interaction between the grafted PEG polymers and the membrane, since the PEGylated NP is highly confined by the membrane after internalization. In this process, the specific ligand-receptor interaction ΔF_{lig} provides the major driving force for the PEGylated NP to be wrapped around and finally enveloped by the membrane. If the energy barriers created by the bending of membrane ΔF_{memb} and conformational free energy loss of tethered chains ΔF_{poly} cannot be overcome by the ligand-receptor interaction ΔF_{lig}, such as $\Delta F_{\text{lig}} < \Delta F_{\text{memb}} + \Delta F_{\text{poly}}$, the endocytosis cannot be accomplished. According to our previous study of spherical NPs,[28] the conformational free energy loss of the grafted PEG polymers can play a very important role during this process. Therefore, we start analyzing the free energy change of grafted PEG polymers ΔF_{poly}.

To determine the free energy change of tethered polymers during endocytosis, the SCF theory given in Section 2.2 has been adopted. According to the SCF theory, the ΔF_{poly} can be decomposed into two parts: one is the elastic energy change ΔF_{el} and the other is the interaction energy change ΔF_{int}. ΔF_{el} is related to the stretching/extension of tethered chains, and qualitatively well approximated by the mean squared end-to-end distances of chains in view of the above-mentioned Flory theory. It can be easily estimated via this route, but we prefer to extract F_{el} via the particular second moment $\langle r^2 \rangle$ of the volume fraction profile. ΔF_{int}, on the other hand, is poorly described by the Flory expression that implies a homogeneous situation (in both unwrapped and wrapped configurations), and definitely requires the volume fraction field $\phi(\mathbf{r})$ of PEG monomers in the space, making it potentially harder to be determined. The cross-sectional views of the volume fraction ϕ for PEG monomers at grafting density 1.6 chains/nm^2, before and after endocytosis, are given in Fig. 6 to study origins of $\Delta F_{\text{poly}} = \Delta F_{\text{el}} + \Delta F_{\text{int}}$. Before the PEGylated NPs are wrapped by the membrane, the tethered PEG monomers are more or less homogeneously distributed around the surfaces of NPs, to reduce their steric interactions. High local volume fractions of PEG monomers are mostly found nearby the cores of PEGylated NPs at this high grafting density. However, after internalization, the distributions of PEG monomers in the space have been dramatically changed.

The structural rearrangement during endocytosis, quantified by $\phi(\mathbf{r})$, gives rise to partially opposing effects. First, the occupied space of PEG monomers has been globally reduced, since the tethered chains are not only confined by the core, but also constrained by the surrounding membrane. Thus, at first glance,

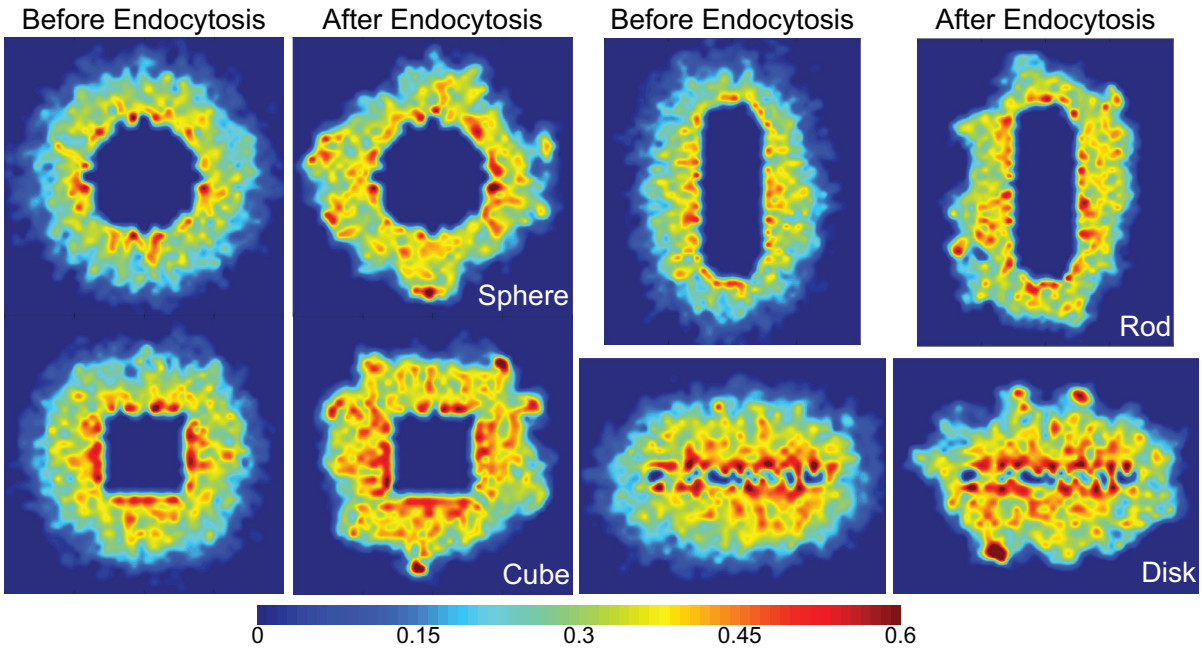

Fig. 6 Cross-sectional views on the PEG volume fraction distributions of differently shaped NPs with grafting density 1.6 chains/nm^2.

the mean extension of tethered chains should have been reduced, implying a negative change of elastic energy $\Delta F_{\rm el} < 0$, while the mean density has increased, suggesting $\Delta F_{\rm int} > 0$. Second, high local volume fractions of PEG monomers after endocytosis not only occur at the tethering surface but also on the outer surface regions of polymer-coated NPs. The corresponding change of the volume fraction profile to larger r values gives rise to $\Delta F_{\rm el} > 0$, and also $\Delta F_{\rm int} > 0$ due to the functional form of the mixing free energy density $f_m(\phi)$. While $\Delta F_{\rm int} > 0$ for both reasons, the sign of $\Delta F_{\rm el}$ will be seen to depend on the grafting density.

As aforementioned, the free ends of grafted PEG chains are bounded with targeting moieties, which can recognize and bind with receptors expressed over the surface of the membrane. After the PEGylated NPs has been fully wrapped by the membrane, the free ends of tethered chains are also bound to the surface of the membrane, due to the specific ligand-receptor interactions. Some of these free ends, and their corresponding tethered chains, can be very close to each other, if their bonded receptors are close. Therefore, the local volume fraction of PEG monomers can be very large in these regions, denoted by the 'hot spots' around NP surfaces given in Fig. 6. Overall, due to the rearrangement of PEG monomers after endocytosis, their volume fraction distributions change from a rather homogeneous state to an inhomogeneous state, as given in Fig. 6. Very much the same principles we detect for PEGylated NPs with lower grafting densities, such as 0.6 and 1.2 chain/nm^2 (see ESI Figs. S9-S10).

The change of extension for tethered chains has been quantified by calculating $\Delta\langle r^2\rangle^{1/2}$ (cf. Fig. 7(a)), defined by the difference of $\langle r^2\rangle^{1/2}$ before and after internalization of PEGylated NPs. When the grafting density σ_p is larger than 0.6 chains/nm^2, the extension $\langle r^2\rangle^{1/2}$ has been reduced by 0.15–0.6 nm for fully internalized NPs, as they are wrapped and confined by the cell membrane (cf. Fig. 3). However, when $\sigma_p < 0.6$ chains/nm^2, most of the grafted PEG polymers have been stretched, as reflected by an increased extension $\Delta\langle r^2\rangle^{1/2} = 0.15$–$0.9$ nm. As demonstrated in Figs. 3-4, the tethered chains have been stretched to enable the targeting moieties (conjugated on their free ends) to bind with receptors at the membrane bending stage. For most of PEGylated NPs with $\sigma_p < 0.6$ chains/nm^2, they cannot be fully internalized (cf. Fig. 4 and ESI Figs. S5-S8) and still stay at the membrane bending stage. Therefore, the grafted PEG polymers are mainly stretched, rather than compressed, due to the specific ligand-receptor binding. According to SCF (Section 2.2) and Flory theory (Section 2.3), the change of elastic energy $\Delta F_{\rm el}$ is related to the stretching/compression of tethered chains. The obtained $\Delta F_{\rm el}$ per chain is given in Fig. 7(b). In accord with our previous observations on spherical NPs, $\Delta F_{\rm el}$ has been mostly enlarged by 0-1 $k_{\rm B}T$ per chain for $\sigma_p < 0.6$ chains/nm^2, while it has been reduced by 0-0.5 $k_{\rm B}T$ per chain for $\sigma_p > 0.6$ chains/nm^2. Interestingly, the NP shape does not seem to play an important role in $\Delta F_{\rm el}$, as the values of $\Delta F_{\rm el}$ are very close to each other for differently shaped NPs.

The change of interaction energy between tethered chains $\Delta F_{\rm int}$ is shown in Fig. 7(c). As the PEGylated NPs are wrapped around by the membrane during endocytosis, the PEG monomers have more chance to interact with each other during this process (cf. Fig. 6). Therefore, $\Delta F_{\rm int}$ has been increased by 0.25–2.0 $k_{\rm B}T$, no matter the PEGylated NPs are fully or partially wrapped by the membrane. Similar to the change of elastic energy $\Delta F_{\rm el}$, the values of $\Delta F_{\rm int}$ for differently shaped NPs are also very close to each other, for a given grafting density, indicating the NP shape does not play an important role here. After $\Delta F_{\rm el}$ and $\Delta F_{\rm int}$ have been determined, the free energy change of grafted PEG polymers $\Delta F_{\rm poly}$ can be readily obtained as $\Delta F_{\rm poly} = \Delta F_{\rm el} + \Delta F_{\rm int}$. As both

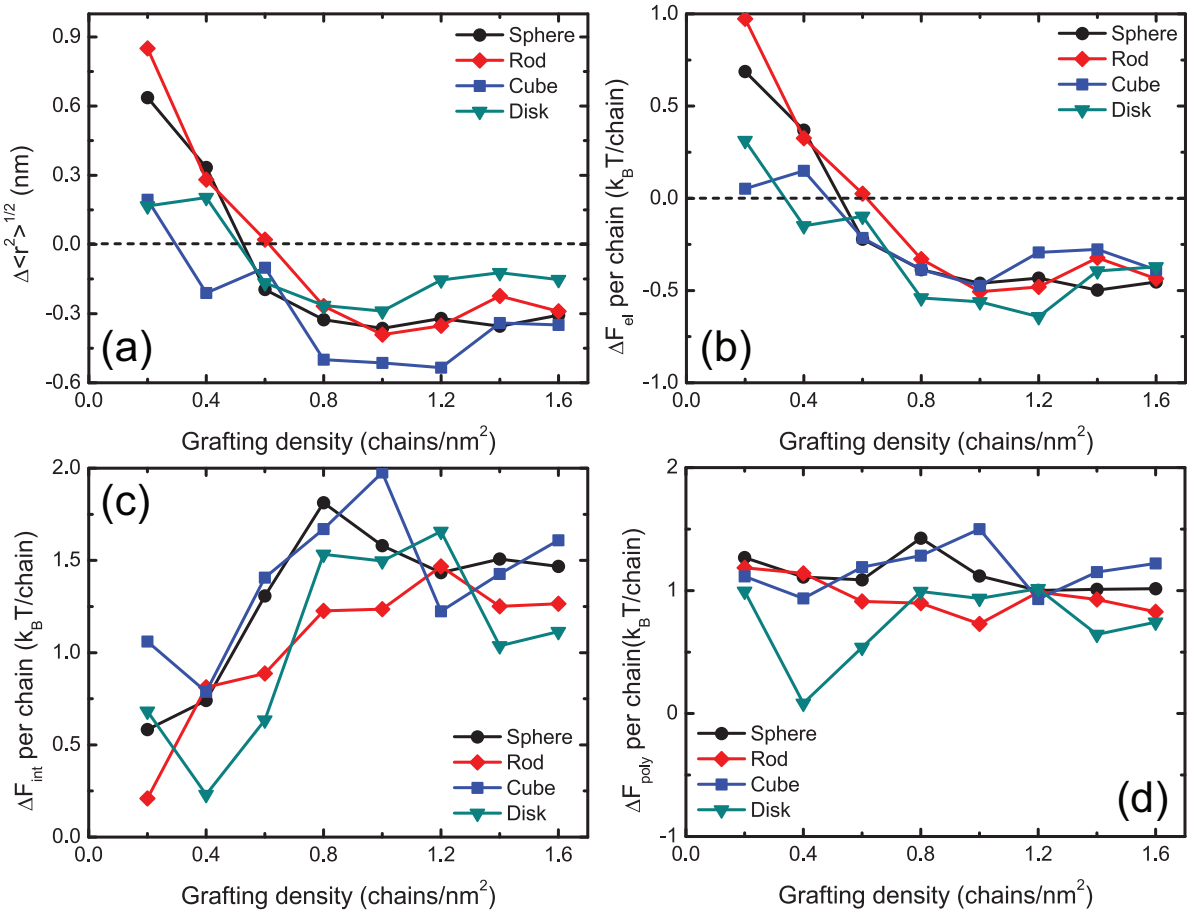

Fig. 7 Grafting density effect on (a) change of extension for tethered chains $\Delta\langle r^2\rangle^{1/2}$, (b) change of elastic energy ΔF_{el}, (c) change of interaction energy ΔF_{int} and (d) change of free energy ΔF_{poly} for tethered PEG polymers, before and after endocytosis. Note that endocytosis cannot be fully accomplished for spherical and cubic NPs with grafting densities 0.2-0.4 chains/nm^2, and also rod- and disk-like NPs with grafting densities 0.2-0.6 chains/nm^2. For these cases the shown values reflect statistical properties of the incompletely wrapped state. The magnitude of the related statistical error is about 0.2 k_BT/chain for all cases, obtained from 5 independent runs.

ΔF_{el} and ΔF_{int} are not sensitive to the shapes of NPs, ΔF_{poly} is also not affected too much by the NP shape, as presented in Fig. 7(d). ΔF_{poly} per chain is found to be around 1 k_BT for all PEGylated NPs, regardless of the NP shape or grafting density. Therefore, the total free energy change $M\Delta F_{poly}$ of the investigated M tethered PEG polymers is in the range of 40–322 k_BT, depending on the number of grafted chains. These values are also close to the free energy change of tethered chains for PEGylated spherical NPs with $N_p = 18$.[28]

3.4 Entry angle effect

According to existing experimental[70] and computational[54] studies, the internalization rate of anisotropic NPs is dependent on their entry angle when approaching the membrane. In our present simulations, the rod- and disk-like NPs approach the membrane with their largest contact areas at the beginning (cf. Figs. 3-4), which enables them to be rapidly accepted by the cell due to the strong ligand-receptor interactions. To explore the entry angle effect of PEGylated NPs, we next study the endocytosis of NPs with comparably small contact areas, as given in Fig. 8. For the rod-like NP, the long axis of rotational symmetry is initially perpendicular to the surface of the membrane, which greatly reduces the interaction between the conjugated targeting moieties and the receptors. To allow more and more targeting moieties on the NP surface to bind with receptors expressed over the surface of the membrane, the rod-like NP continuously rotates until it completely resides within a plane locally tangential to the membrane surface during the membrane bending stage (at t = 0–0.7 μs in Fig. 8). Hereafter, the upper leaflet of the lipid bilayer starts to protrude and wrap around the NP surface, until the rod-like NP is completely enveloped by the membrane. For the disk-like NP, it also takes about 0.73 μs to rotate and completely lay down on the membrane surface during the membrane bending stage (cf. Fig. 8). In contrast, the internalization of the disk-like NPs follows the membrane monolayer protruding stage and equilibrium stage, as presented in Fig. 8 (additional details provided by ESI Figs. S11-S12).

Comparing with the results given in Fig. 3, the entry angle does actually play an important role during the internalization process of these anisotropic NPs. As these NPs approach the membrane

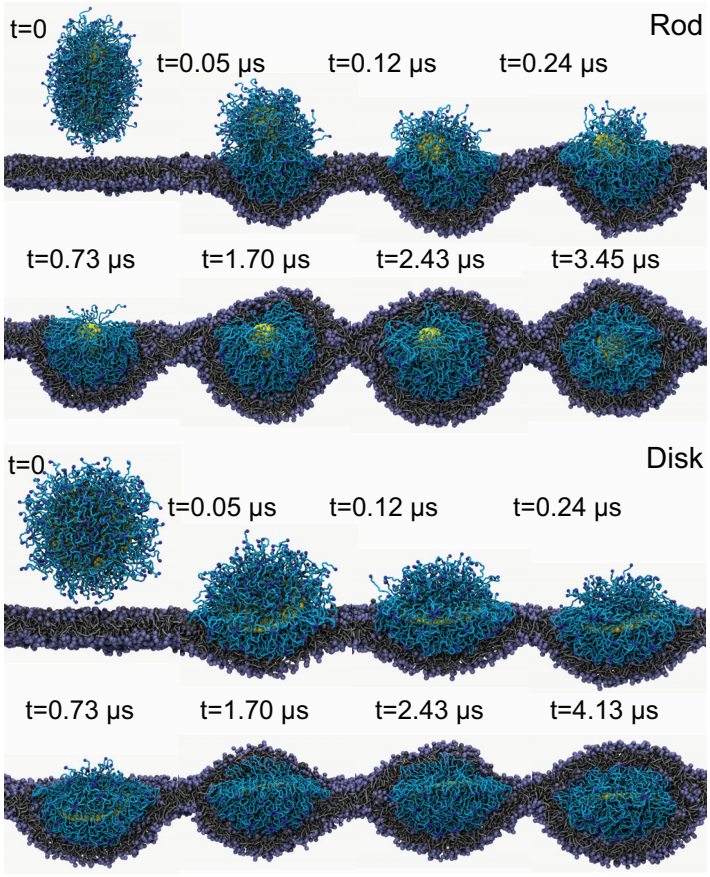

Fig. 8 Entry angle effect on endocytosis kinetics of rod- and disk-like NPs with grafting density 1.6 chains/nm^2. The color scheme is the same as Fig. 3. The complicated rotations of these PEGylated NPs have been observed, especially during the membrane bending stage ($0 < t < 0.73$ μs).

surface with largest contact areas, they do not need to rotate and lay down on the membrane surface to allow more targeting moieties to bind with receptors. However, if these NPs dock the membrane with their smallest contact areas, they need extra time to rotate and lay down for targeting moieties binding with receptors. In this way, the entry angles of anisotropic NPs can greatly affect their internalization rate. For example, it takes about the 2.55 μs for the rod-like NPs to be internalized with horizontal docking position, while it has been increased to 3.45 μs for the same NP with vertical docking position. The internalization rate has been reduced by 35%. Similarly, the endocytosis rate of disk-like NP can be reduced by 49%, due to the different docking positions. These results further confirm that the entry angle of anisotropic NPs greatly affects their endocytosis kinetics, as already suggested by previous studies.[54,70,71] The reorientation times are quantitatively determined by the friction tensor coefficients characterizing the polymer-coated NP shape. Such calculations are available for convex particles including cuboidal (including cubic), cylindrical (including rod-like) and ellipsoidal (including disk-like and spherical) shapes dissolved in a structureless viscous medium[72] and in connection with phoretic forces for rarefied, less dense systems.[73]

4 Discussion

To unambiguously clarify the effect of shape on the cellular uptake of PEGylated NPs, we systematically study differently shaped NPs, such as sphere, rod, cube and disk with identical surface areas, same amounts of grafted PEG polymers and identical ligand-receptor interaction strengths. Based on large scale molecular simulations results, we find that the internalization rate of spherical NPs is the highest, followed by cubic NPs, then rod-like and finally disk-like NPs. Upon choosing the internalization rates of spherical NPs as a reference quantity, only 87% of cubic, 77% of rod-like, and 65% of disk-like NPs are taken up during the amount of time required for a spherical NP to be fully internalized. If the entry angle effect of anisotropic NPs (such as rod and disk) is considered (cf. Fig. 8), the cellular uptake efficiency of rod-like and disk-like NPs can be further reduced. Thus, the spherical NPs serve as the most efficient vectors to deliver the drug molecules into the diseased cells, compared with non-spherical counterparts. Not only we didn't find any evidence that non-spherical shapes help to establish ligand-receptor bindings in locations that may lead to a reduction of the free energy cost related to the structural reorganization of the polymer brush. In addition the sphere is the only homogeneous shape that cannot suffer from reorientation issues. Importantly, we reached this conclusion by variation of shape while keeping all other parameters, that may potentially affect the internalization process, constant.

The endocytosis kinetics of naked NPs with different shapes has been computationally studied before. Li et al. explored the shape anisotropic effect on internalization of ligand-coated NPs (without PEGylation), including spherical, cylindrical and disk-shaped NPs.[54] The spherical NPs were found to display the fastest endocytosis rate, while the rate for cylindrical NPs was relatively slower, and the disk-like NPs exhibited the slowest endocytosis rate. This ordering is mainly induced by the different membrane bending energies: the spherical NPs only need to overcome the minimum elastic bending energy, but the disk-like NPs involve a stronger membrane deformation and complicated rotations of NPs are required.[54] In these studies, the differently shaped NPs did not have equal surface area or volume. Nevertheless, the obtained trend agrees reasonably well with the findings of the present study, suggesting an important role of the underlying NP shape. Huang et al. studied the receptor-mediated endocytosis of ligand-coated but otherwise naked NPs with various shapes,[49] such as spherical and rod-like NPs with different aspect ratios, again with unmatched surface areas or volumes. Within these studies the wrapping time for a spherical NP to be fully enveloped by the membrane was only about 77% of that for a rod-like NP with aspect ratio $\rho = 1 + \mathscr{L}_{\rm rod}/2\mathscr{R}_{\rm rod} = 2$.[49] All these simulation results on ligand-coated NPs (without PEGylation) are in good agreement with our results on PEGylated NPs, ultimately revealing the spherical NPs as the more efficient therapeutic carriers.

The NP shape effect has also been explored through experiments. Chan and co-workers have studied the cellular uptake of spherical and rod-like Au NPs, whose surfaces were stabilized by citric acid ligands to avoid their aggregation.[17] The number of Au NPs taken up per HeLa cell were about 3×10^3 and $1.5–2.0\times10^3$

for spherical NPs with radius $\mathscr{R}_{\text{sphere}} = 7$ nm and rod-like NPs with radius $\mathscr{R}_{\text{rod}} = 7$ nm and length $\mathscr{L}_{\text{rod}} = 26$ nm, respectively. Thus, the cellular uptake efficiency for rod-like NPs is only about 50–67%, compared with their spherical counterparts. Xia and co-workers have investigated the internalization of Au NPs with different sizes, shapes and surface functional groups.[26] Spherical NPs with radii $\mathscr{R}_{\text{sphere}} = 7.5$ and 22.5 nm, and cubic NPs with side lengths $\mathscr{L}_{\text{cube}} = 33$ and 55 nm were investigated. The surfaces of these PEGylated NPs are tethered by PEG polymers with their free ends conjugated by anti-HER2 targeting moieties, which is similar to the PEGylated NP models studied in present work. Through receptor-mediated endocytosis, they found that >90% of spherical NPs can be internalized by SK-BR-3 breast cancer cells, while only 70–80% cubic NPs were taken up. Muzykantov and co-workers experimentally measured the endocytosis kinetics of spherical and disk-like particles for endothelial targeting.[68] Their particles are made by polystyrene and their surfaces are coated by anti-ICAM ligands for specific targeting endothelial cells (ECs). The radii of the spherical particles are about $\mathscr{R}_{\text{sphere}} =$ 0.1, 0.5, 1, 5 and 10 μm, while the elliptical disk has dimension $0.1 \times 1 \times 3$ μm. The experimental results revealed that the ECs endocytosed 5 μm spheres as fast as 0.1 μm spheres, at 81.4 $\pm$ 2.8% and 94.2 $\pm$ 2.9% internalization after 1 hour, respectively, and $t_{1/2} \simeq 15$ minutes in both cases.[68] Although the disks were also internalized by ECs, their endocytosis kinetics was remarkably slower as $t_{1/2} \simeq 1$ hour. Therefore, the cellular uptake efficiency of disks is only about 40-50% of their spherical counterparts.[68]

To summarize above observations, the different cellular uptake efficiencies for differently shaped NPs are plotted in Fig. 5(b). Interestingly, our present simulation results are in good agreement with existing computational[49,54] and experimental[17,26,68] studies, although different sizes, surface properties and compositions (materials) of NPs were considered, highlighting the key role played by the NP shape. It also raises the most important question: *Does the shape of a NP play a role during endocytosis?*

As we have discussed in Section 3.3, the internalization of PEGylated NPs relies on the competition between ligand-receptor interaction ΔF_{lig}, membrane bending energy ΔF_{memb} and conformational entropy loss of tethered PEG polymers ΔF_{poly}. To understand the NP shape effect, it is important to clarify these free energy changes. In Section 3.3, ΔF_{poly} for differently shaped NPs has been studied through our SCF theory, indicating the NP shape does not significantly affect ΔF_{poly}. The free energy released by the ligand-receptor binding ΔF_{lig} can be easily determined as $\Delta F_{\text{lig}} = M \times F_{\text{LR}}$, where M and F_{LR} are the number of tethered chains (targeting moieties) and ligand-receptor interaction strength, respectively. Here we consider that all the free ends have been conjugated by targeting moieties, closely mimicking the experimental conditions.[25,26] Thus, the number of targeting moieties is the same as the number of grafted PEG polymers. The specific ligand-receptor interaction, prescribed by a modified Lennard-Jones potential as given in our previous study of spherical NPs,[28] is fixed to be $F_{\text{LR}} = 7.65 k_{\text{B}}T$. Since all the NPs have equal surface area and are compared under the same grafting density (number of tethered chains) and ligand-receptor binding strength, ΔF_{lig} does not depend on the NP shape. Therefore, ΔF_{memb} must be the key to explain why the internalization rate of PEGylated NPs is shape dependent. A second shape-dependent mechanism that affects the internalization rate, and that we discussed above, is orientational relaxation behavior for anisotropic NPs.

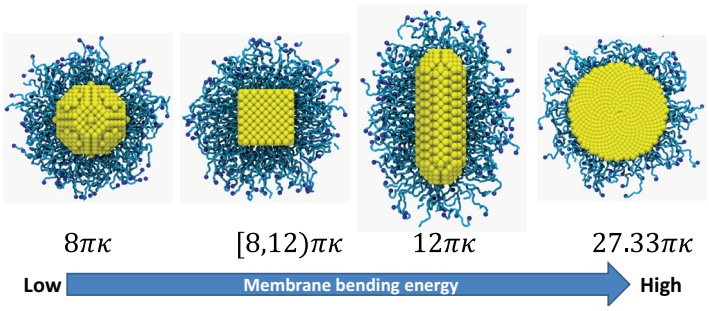

Fig. 9 Membrane bending energy for different shaped NPs. κ is the bending curvature modulus of the membrane.

The membrane bending energy ΔF_{memb} can be quantified by the Helfrich-Canham-Evans free energy.[74] As given in ESI section 7, $\Delta F_{\text{memb}} = 8\pi\kappa$ for spherical NPs, regardless of their radii. Here κ is the bending curvature modulus of the membrane, which is typically in the order of $20 k_{\text{B}}T$.[75] For rod-like NPs with two hemispherical caps joined by a cylinder, $\Delta F_{\text{memb}} = 8\pi\kappa + \pi\kappa \mathscr{L}_{\text{rod}}/\mathscr{R}_{\text{rod}}$, where $\mathscr{L}_{\text{rod}}$ is the length of the cylinder and $\mathscr{R}_{\text{rod}}$ is the radius of both the cylinder and hemispherical cap. For the case of $\mathscr{L}_{\text{rod}}/\mathscr{R}_{\text{rod}} = 4$, we have $\Delta F_{\text{memb}} = 12\pi\kappa$ for rod-like NPs. For cubic and disk-like NPs, it is hard to directly calculate ΔF_{memb}, since their shapes are rather complicated. By assuming endosomal shapes of these NPs, we can determine $\Delta F_{\text{memb}} = 12\pi\kappa$ and $27.33\pi\kappa$ (see ESI section 7). However, by closely inspecting the vesicle shapes, we find that the endosome for cubic NPs is very similar to a sphere (cf. Figs. 3-4), due to the appearance of grafted PEG polymers. Thus, $\Delta F_{\text{memb}} \in [8, 12)\pi\kappa$ for cubic NPs. According to these values, the spherical NPs encounters the minimal bending energy barrier, followed by the cubic NPs, then rod- and disk-like NPs, as given in Fig. 9. This order is exactly the same as the cellular uptake efficiency given in Fig. 5(b), which further conforms that the different membrane bending energy is the major reason for the observed NP shape effect.

In recent years, Au star-shaped NPs have been recognized as promising cargos for drug- and gene-delivery.[76–78] The method developed in the present study can also be applied to study the internalization of PEGylated complex-shaped, and in particular star-shaped NPs, as demonstrated in ESI section 8. Comparing 6 arms star-shaped NPs with our four basic NP geometries at identical surface area, identical amount of tethered PEG chains and same ligand-receptor interaction strength, we find that the wrapping time of a star-shaped NPs is very close to the one we obtained for the spherical NP (cf. ESI Figs. S15-S16). Therefore, both the star-shaped and spherical NPs should demonstrate high efficacy for drug-delivery, as suggested by experimental results,[77], and further confirmed by our simulation results. It is not difficult to understand this phenomenon, as both geometries are highly sym-

metric, indicating that they will encounter a similar membrane bending energy during endocytosis.

Although the different internalization rates for differently shaped NPs are induced by the different elastic bending energies of the membrane, the grafted PEG polymer eventually plays an important role. First, according to experimental studies,[24–26] the targeting moieties are mostly conjugated on the free ends of tethered chains. Thus, high grafting densities of PEG provide more free ends to be bound with these targeting moieties, which can reduce the time for PEGylated NPs to be accepted by the diseased cell (cf. Fig. 5). Second, the effective shape of NPs is changed by its tethered polymers, with a corresponding effect on the membrane bending energy. As shown in Fig. 1 and Figs. S1-S4, at high grafting densities such as 1.6 chains/nm^2, the surfaces of differently shaped cores are fully covered by PEG polymers. The effective shapes of the cubic, rod- and disk-like NPs are more or less spherical. Especially for the cubic NP, the vesicle wrapped around its surface is basically spherical, thus reducing the elastic bending energy significantly from $12\pi\kappa$ to $8\pi\kappa$, as aforementioned. For rod-like NPs, the membrane bending energy can also be reduced to $\Delta F_{\rm memb} = 8\pi\kappa + \pi\kappa\mathscr{L}_{\rm rod}/(\mathscr{R}_{\rm rod}+R)$, assuming the PEG polymers are uniformly coated on the NP surface with thickness R. Given the extensions of PEG polymers (cf. Fig. 2), the membrane bending energy will be reduced from $12\pi\kappa$ to $9.35\pi\kappa$. The shape of the disk-like NP is also changed from a disk to a prolate ellipsoid, at high grafting densities. Thus, the corresponding membrane bending energy will be reduced from $27.33\pi\kappa$ down to $13\pi\kappa$.[71] Considering the dramatic reduction of the membrane bending energy for these PEGylated NPs at high grafting densities (such as 1.2-1.6 chains/nm^2), their internalization rates should also become very close to each other, as presented in Fig. 5(a). It is in the limit of both high grafting density and molecular weight of the PEG chains, that all NPs covered by an identical large amount of PEG monomers will ultimately approach the same size, the same spherical shape, and behave identical.

In the present study we set our focus on differently shaped NPs with equal surface areas of their cores. We may then ask: *If or how does the endocytosis behavior of differently shaped NPs changes under the constraint of equal core volume (but different surface area)?* In an attempt to address this question, let us consider the differently shaped NPs, sphere, rod, cube and disk, with the core radius of the spherical NP fixed to be $\mathscr{R}_{\rm sphere} = 4$ nm. Then, $\mathscr{R}_{\rm rod} =$ 2.52 nm and $\mathscr{L}_{\rm rod} = 10.08$ nm for the rod-like NP with aspect ratio $\rho = 3$. The side length of the cubic NP is $\mathscr{L}_{\rm cube} = 6.45$ nm. The thickness of the disk $2p$ and its radius $\mathscr{R}_{\rm disk}$ are 0.95 and 9.5 nm, respectively, by assuming that its thickness is about $1/10$ of its radius. This way, all the cores have identical volume 268 nm^3. The surface areas for these cores are 201.1, 239.4, 249.6 and 623.8 nm^2 for the sphere, rod, cube and disk, respectively. If we assume that these NPs exhibit the same amount of grafted PEG polymers (implying different grafting densities) and ligand-receptor interactions, the membrane bending energies are $8\pi\kappa$, $12\pi\kappa$, $[8,12)\pi\kappa$ and $17.2\pi\kappa$ for the sphere, rod, cube and disk, respectively. The sphere and disk encounter the minimal and maximum membrane bending energies, respectively. Therefore, the spherical and disk-like NP should exhibit the fastest and slowest internalization rates, respectively, which still follows our previous conclusion. However, if instead an identical grafting density is considered, these NPs will have different amounts of tethered chains, a different free energy change of these chains during endocytosis, and a different ligand-receptor binding strength. In that case, the NP shape effect cannot be quantitatively deduced using the currently available results due to the complex interplay between size, shape and surface property of these NPs.

Finally, we should emphasize that our present study focuses on the binding of NPs to the membrane surface and their subsequent budding behavior. As mentioned in the Introduction, the overall drug delivery efficacy also relies on the endosomal release of the wrapped NPs. Vácha *et al.* have explored the endosomal release through changing the ligand-receptor binding strength after wrapping.[79] The NP release is found to be not only affected by the bending curvature modulus, but also influenced by the Gaussian modulus and lateral tension of the membrane. Thus, the effect of NP shape on the endosomal release can be expected to be more complicated, and still remains to be explored independently. In short, the efficacy of NP-mediated drug delivery relies on the binding of NPs to the cell surface, subsequent budding, pinching off and related endosomal release. All these factors should be systematically considered.

5 Conclusion

In summary, large scale DPD simulations have been performed to study the NP shape effect during internalization of PEGylated NPs, by considering differently shaped convex NP cores such as sphere, rod, cube and disk. Imposing the conditions of equal surface areas of the cores, same amount of tethered PEG polymers and identical ligand-receptor binding strength, the NP shape effect has been unambiguously clarified. The spherical NPs exhibit the fastest endocytosis rate, followed by cubic NPs, then rod- and disk-like NPs. The internalization of anisotropic NPs, such as rod and disk, can be further delayed by an unfavorable docking orientation, since a time-consuming rotation is required to achieve alignment. Through a detailed free energy analysis, the NP shape effect has been identified to be mainly induced by the membrane bending energy change: spherical NPs encounter the minimal membrane bending energy change, while disk-like NPs involve a stronger deformation of the membrane and exhibit the maximal membrane bending energy change. The conformational free energy loss of tethered PEG polymers during endocytosis is found to be in the order of a single $k_{\rm B}T$ per chain, via our SCF theory, regardless of the NP shape. Thus, the effect of shape on the internalization rate of PEGylated NPs is governed by the membrane bending energy, when the grafting density of PEG polymers is lower than 1.2 chains/nm^2. However, if the grafting density is higher, such as 1.2–1.6 chains/nm^2, the surfaces of the cores of PEGylated NPs are fully covered and shielded by the tethered chains. Under such conditions, the shapes of the cores are basically invisible to the cell membrane, which can significantly reduce the energy barrier caused by membrane bending. Accordingly are the internalization rates of the differently shaped NPs close to each other, indicating that the NP shape effect has been dramatically weakened at high grafting densities of

PEG polymers. All these findings are useful in providing quantitative guidelines and design principles for improved drug delivery systems.

For example, increasing attention had recently been given to the study of highly branched structures such as dendrimers and star polymers with the hope that interesting effects of architecture on biological properties may be discovered. Dendronized linear polymers, that attain extended conformations and can be described as somewhat rigid, cylindrical rods[80] may be interesting scaffolds for drug delivery as the large number of functionalizable peripheral groups on the dendrons should allow for very high levels of drug loading.[81] Our current study suggests that spherical dendrimers rather than dendronized polymers should be more efficient concerning the internalization efficiency, because dendronized polymers cannot be coated with linear polymers without loosing all their advantages. On the other hand, there seems to be a positive correlation between size of a dendronized polymer and its blood circulation time. A long-circulating nature is advantageous for the development as drug carriers.[81]

Acknowledgements

The support of this research by National Science Foundation (NSF) is gratefully acknowledged. Y.L. warmly thanks the financial support provided by Ryan Fellowship and Royal E. Cabell Terminal Year Fellowship at Northwestern University. W.K.L. expresses thanks for the support from AFOSR Grant No. FA9550-14-1-0032. This research was supported in part through the computational resources and staff contributions provided for the Quest high performance computing facility at Northwestern University which is jointly supported by the Office of the Provost, the Office for Research, and Northwestern University Information Technology.

References

1 K. Cho, X. Wang, S. Nie and D. M. Shin, *Clin. Cancer Res.*, 2008, **14**, 1310–1316.

2 J. Siepmann, R. A. Siegel and M. J. Rathbone, *Fundamentals and applications of controlled release drug delivery*, Springer, 2012.

3 W. H. De Jong, W. I. Hagens, P. Krystek, M. C. Burger, A. J. A. M. Sips and R. E. Geertsma, *Biomaterials*, 2008, **29**, 1912–1919.

4 M. L. Immordino, F. Dosio and L. Cattel, *Int. J. Nanomed.*, 2006, **1**, 297.

5 R. H. Muller and C. M. Keck, *J. Biotechnol.*, 2004, **113**, 151–170.

6 V. P. Torchilin, *Nanoparticulates as drug carriers*, Imperial college press, 2006.

7 D. C. Drummond, O. Meyer, K. Hong, D. B. Kirpotin and D. Papahadjopoulos, *Pharmacol. Rev.*, 1999, **51**, 691–744.

8 T. M. Allen and P. R. Cullis, *Science*, 2004, **303**, 1818–1822.

9 A. Gabizon and D. Papahadjopoulos, *Proc. Natl. Acad. Sci. USA*, 1988, **85**, 6949–6953.

10 V. P. Torchilin, *Nat. Rev. Drug Discovery*, 2005, **4**, 145–160.

11 P. Alivisatos, *Nat. Biotechnol.*, 2003, **22**, 47–52.

12 M. Ferrari, *Nat. Rev. Cancer*, 2005, **5**, 161–171.

13 G. Bao, Y. Bazilevs, J.-H. Chung, P. Decuzzi, H. D. Espinosa, M. Ferrari, H. Gao, S. S. Hossain, T. J. R. Hughes, R. D. Kamm, W. K. Liu, A. Marsden and S. B, *J. R. Soc. Interface.*, 2014, **11**, 20140301.

14 M. Dellian, F. Yuan, V. S. Trubetskoy, V. P. Torchilin and R. K. Jain, *Br. J. Cancer*, 2000, **82**, 1513–1518.

15 S. K. Hobbs, W. L. Monsky, F. Yuan, W. G. Roberts, L. Griffith, V. P. Torchilin and R. K. Jain, *Proc. Natl. Acad. Sci. USA*, 1998, **95**, 4607–4612.

16 W. Jiang, B. Y. S. Kim, J. T. Rutka and W. C. W. Chan, *Nat. Nanotechnol.*, 2008, **3**, 145–150.

17 B. D. Chithrani, A. A. Ghazani and W. C. W. Chan, *Nano Lett.*, 2006, **6**, 662–668.

18 P. Decuzzi, R. Pasqualini, W. Arap and M. Ferrari, *Pharm. Res.*, 2009, **26**, 235–243.

19 P. Decuzzi and M. Ferrari, *Biomaterials*, 2008, **29**, 377–384.

20 H. Shmeeda, D. Tzemach, L. Mak and A. Gabizon, *J. Controlled Release*, 2009, **136**, 155–160.

21 R. Gref, M. Lück, P. Quellec, M. Marchand, E. Dellacherie, S. Harnisch, T. Blunk and R. H. Müller, *Colloids Surf., B*, 2000, **18**, 301–313.

22 S. D. Perrault, C. Walkey, T. Jennings, H. C. Fischer and W. C. W. Chan, *Nano Lett.*, 2009, **9**, 1909–1915.

23 P. Nativo, I. A. Prior and M. Brust, *ACS Nano*, 2008, **2**, 1639–1644.

24 E. Oh, J. B. Delehanty, K. E. Sapsford, K. Susumu, R. Goswami, J. B. Blanco-Canosa, P. E. Dawson, J. Granek, M. Shoff, Q. Zhang, P. L. Goering, A. Huston and I. L. Medintz, *ACS Nano*, 2011, **5**, 6434–6448.

25 H. Chen, H. Paholak, M. Ito, K. Sansanaphongpricha, W. Qian, Y. Che and D. Sun, *Nanotechnology*, 2013, **24**, 355101.

26 E. C. Cho, L. Au, Q. Zhang and Y. Xia, *Small*, 2010, **6**, 517–522.

27 L. Tang, X. Yang, Q. Yin, K. Cai, H. Wang, I. Chaudhury, C. Yao, Q. Zhou, M. Kwon, J. A. Hartman, I. T. Dobrucki, L. W. Dobrucki, L. B. Borst, S. Lezmig, W. G. Helferich, A. L. Ferguson, T. M. Fan and J. J. Cheng, *Proc. Natl. Acad. Sci. USA*, 2014, **111**, 15344–15349.

28 Y. Li, M. Kröger and W. K. Liu, *Biomaterials*, 2014, **35**, 8467–8478.

29 X. Xia, M. Yang, Y. Wang, Y. Zheng, Q. Li, J. Chen and Y. Xia, *ACS Nano*, 2011, **6**, 512–522.

30 B. Tang, S. Xu, J. An, B. Zhao, W. Xu and J. R. Lombardi, *Phys. Chem. Chem. Phys.*, 2009, **11**, 10286–10292.

31 X. Xia and Y. Xia, *Front. Phys.*, 2014, **9**, 378–384.

32 G. J. Doherty and H. T. McMahon, *Annual review of biochemistry*, 2009, **78**, 857–902.

33 I. Canton and G. Battaglia, *Chemical Society Reviews*, 2012, **41**, 2718–2739.

34 P. J. Hoogerbrugge and J. M. V. A. Koelman, *Europhys. Lett.*, 1992, **19**, 155.

35 J. M. V. A. Koelman and P. J. Hoogerbrugge, *Europhys. Lett.*, 1993, **21**, 363.

36 R. D. Groot and K. L. Rabone, *Biophys. J.*, 2001, **81**, 725–736.
37 T. Yue and X. Zhang, *ACS Nano*, 2012, **6**, 3196–3205.
38 R. Guo, J. Mao and L.-T. Yan, *ACS Nano*, 2013, **7**, 10646–10653.
39 M. Venturoli, M. M. Sperotto, M. Kranenburg and B. Smit, *Phys. Rep.*, 2006, **437**, 1–54.
40 H.-M. Ding and Y.-Q. Ma, *Biomaterials*, 2012, **33**, 5798–5802.
41 Y. Li, H. Yuan, A. von dem Bussche, M. Creighton, R. H. Hurt, A. B. Kane and H. Gao, *Proc. Natl. Acad. Sci. USA*, 2013, **110**, 12295–12300.
42 J. Mao, R. Guo and L.-T. Yan, *Biomaterials*, 2014, **35**, 6069–6077.
43 Y. Li, X. Li, Z. Li and H. Gao, *Nanoscale*, 2012, **4**, 3768–3775.
44 R. Vácha, F. J. Martinez-Veracoechea and D. Frenkel, *Nano Lett.*, 2011, **11**, 5391–5395.
45 K. Yang and Y.-Q. Ma, *Nat. Nanotechnol.*, 2010, **5**, 579–583.
46 H.-M. Ding, W.-D. Tian and Y.-Q. Ma, *ACS Nano*, 2012, **6**, 1230–1238.
47 B. Hong, F. Qiu, H. Zhang and Y. Yang, *J. Phys. Chem. B*, 2007, **111**, 5837–5849.
48 T. Yue, X. Zhang and F. Huang, *Soft matter*, 2014, **10**, 2024–2034.
49 C. Huang, Y. Zhang, H. Yuan, H. Gao and S. Zhang, *Nano Lett.*, 2013, **13**, 4546–4550.
50 H. Lee, A. H. de Vries, S.-J. Marrink and R. W. Pastor, *J. Phys. Chem. B*, 2009, **113**, 13186–13194.
51 A. Malugin and H. Ghandehari, *J. Appl. Toxicol.*, 2010, **30**, 212–217.
52 C. D. Walkey, J. B. Olsen, H. Guo, A. Emili and W. C. W. Chan, *J. Am. Chem. Soc.*, 2012, **134**, 2139–2147.
53 A. de la Zerda, S. Bodapati, R. Teed, S. Y. May, S. M. Tabakman, Z. Liu, B. T. Khuri-Yakub, X. Chen, H. Dai and S. S. Gambhir, *ACS Nano*, 2012, **6**, 4694–4701.
54 Y. Li, T. Yue, K. Yang and X. Zhang, *Biomaterials*, 2012, **33**, 4965–4973.
55 A. Nunes-Alves and G. M. Arantes, *J. Chem. Inf. Model.*, 2014, **54**, 2309–2319.
56 J. C. Shillcock and R. Lipowsky, *Nat. Mater.*, 2005, **4**, 225–228.
57 J. R. Lu, Z. X. Li, R. K. Thomas, E. J. Staples, I. Tucker and J. Penfold, *J. Phys. Chem.*, 1993, **97**, 8012–8020.
58 J. W. Murray and A. W. Wolkoff, *Adv. Drug Delivery Rev.*, 2003, **55**, 1385–1403.
59 J. M. H. M. Scheutjens and G. J. Fleer, *J. Phys. Chem.*, 1979, **83**, 1619–1635.
60 C. M. Wijmans, J. M. H. M. Scheutjens and E. B. Zhulina, *Macromolecules*, 1992, **25**, 2657–2665.
61 E. B. Zhulina, O. V. Borisov and V. A. Priamitsyn, *J. Colloid Interface Sci.*, 1990, **137**, 495–511.
62 A. Halperin, M. Kröger and E. B. Zhulina, *Macromolecules*, 2011, **44**, 3622–3638.
63 C. M. Wijmans and E. B. Zhulina, *Macromolecules*, 1993, **26**, 7214–7224.
64 E. Eisenriegler, *Polymers near surfaces: conformation properties and relation to critical phenomena*, World Scientific, 1993.
65 P. J. Flory, *Statistical mechanics of chain molecules*, Interscience, 1969.
66 M. Kröger, O. Peleg and A. Halperin, *Macromolecules*, 2010, **43**, 6213–6224.
67 P. Decuzzi and M. Ferrari, *Biophys. J.*, 2008, **94**, 3790–3797.
68 S. Muro, C. Garnacho, J. A. Champion, J. Leferovich, C. Gajewski, E. H. Schuchman, S. Mitragotri and V. R. Muzykantov, *Mol. Ther.*, 2008, **16**, 1450–1458.
69 Y. Li, W. Stroberg, T.-R. Lee, H. S. Kim, H. Man, D. Ho, P. Decuzzi and W. K. Liu, *Comput. Mech.*, 2014, **53**, 511–537.
70 S. E. Gratton, P. A. Ropp, P. D. Pohlhaus, J. C. Luft, V. J. Madden, M. E. Napier and J. M. DeSimone, *Proc. Natl. Acad. Sci. USA*, 2008, **105**, 11613–11618.
71 S. Dasgupta, T. Auth and G. Gompper, *Nano Lett.*, 2014, **14**, 687–693.
72 W. A. Wegener, V. J. Koester and R. M. Dowben, *Proc. Natl. Acad. Sci. USA*, 1979, **76**, 6356–6360.
73 M. Kröger and M. Hütter, *J. Chem. Phys.*, 2006, **125**, 044105.
74 U. Seifert, *Adv. Phys.*, 1997, **46**, 13–137.
75 S. Leikin, M. M. Kozlov, N. L. Fuller and R. P. Rand, *Biophys. J.*, 1996, **71**, 2623–2632.
76 D. H. M. Dam, K. S. Culver, P. N. Sisco and T. W. Odom, *Therapeutic delivery*, 2012, **3**, 1263–1267.
77 D. H. M. Dam, K. S. Culver and T. W. Odom, *Mol. Pharmaceutics*, 2014, **11**, 580–587.
78 D. H. M. Dam, K. S. Culver, I. Kandela, R. C. Lee, K. Chandra, H. Lee, C. Mantis, A. Ugolkov, A. P. Mazar and T. W. Odom, *Nanomed. Nanotechnol. Biol. Med.*, 2015, **11**, 671–679.
79 R. Vácha, F. J. Martinez-Veracoechea and D. Frenkel, *ACS nano*, 2012, **6**, 10598–10605.
80 A. D. Schlüter and J. P. Rabe, *Angew. Chem. Int. Ed.*, 2000, **39**, 864–883.
81 C. C. Lee, M. Yoshida, J. M. J. Fréchet, E. E. Dy and F. C. Szoka, *Bioconjugate Chem.*, 2005, **16**, 535–541.